ФИЗИКА ЭЛЕМЕНТАРНЫХ ЧАСТИЦ И АТОМНОГО ЯДРА
2009. Т. 40. ВЫП. 2

PROCESSES IN HIGH-ENERGY HEAVY-ION ACCELERATION

*D. Dinev**

Institute for Nuclear Research and Nuclear Energy,
Bulgarian Academy of Sciences, Sofia, Bulgaria

*E-mail: dinnet@inrne.bas.bg

ФИЗИКА ЭЛЕМЕНТАРНЫХ ЧАСТИЦ И АТОМНОГО ЯДРА
2009. Т. 40. ВЫП. 2

PROCESSES IN HIGH-ENERGY HEAVY-ION ACCELERATION

D. Dinev[*]

Institute for Nuclear Research and Nuclear Energy,
Bulgarian Academy of Sciences, Sofia, Bulgaria

A review of processes that occur in high-energy heavy-ion acceleration by synchrotrons and colliders and that are essential for the accelerator performance is presented. Interactions of ions with the residual gas molecules/atoms and with stripping foils that deliberately intercept the ion trajectories are described in detail. These interactions limit both the beam intensity and the beam quality. The processes of electron loss and capture lie at the root of heavy-ion charge-exchange injection. The review pays special attention to the ion-induced vacuum pressure instability which is one of the main factors limiting the beam intensity. The intrabeam scattering phenomenon which restricts the average luminosity of ion colliders is discussed. Some processes in nuclear interactions of ultrarelativistic heavy ions, that could be dangerous for the performance of ion colliders, are represented in the last chapter.

Представлен обзор процессов, которые имеют место при ускорении тяжелых ионов до высоких энергий синхротронами и коллайдерами и которые в значительной мере определяют параметры ускорителя. Большое внимание уделено процессам взаимодействия ионов с молекулами и атомами остаточного газа и с перезарядными мишенями. Эти взаимодействия ограничивают как интенсивность, так и качество пучков. Процессы потери и/или захвата электронов лежат в основе метода перезарядной инжекции тяжелых ионов. Обсуждается вызванная ионами нестабильность давления остаточного газа. Эта нестабильность давления является одним из основных факторов, ограничивающих интенсивность пучков. Рассматривается внутрипучковое рассеяние ионов. Это явление ограничивает среднюю светимость ионных коллайдеров. В последнем разделе обсуждаются некоторые процессы при ядерных взаимодействиях ультрарелятивистских пучков тяжелых ионов, которые могут ограничивать достижимые параметры ионных коллайдеров.

PACS: 25.75.-q; 29.20.db; 29.20.dk; 52.59.Fn

INTRODUCTION

Historically the investigations with accelerated beams of heavy ions began with nuclear structure studies and with synthesis of new transuranium elements. For these experiments one needs ion energies, which lie slightly above the Coulomb barrier. Tandems, linear ion accelerators and cyclotrons were used at the early times of research with heavy-ion beams. Very soon the scientific

[*]E-mail: dinnet@inrne.bas.bg

interest broadened toward more deep and sophisticated experimental studies in the fields of atomic and nuclear physics and applications in cancer therapy.

When the available ion energy surpassed the 1 GeV/u threshold, studies of the nuclear equation of states and search for very hot and dense nuclear matter and for phase transitions began.

In this review we will restrict ourselves to the problems of acceleration of heavy ions to relativistic energies, i.e., to more than 1 GeV/u. This is done by synchrotrons.

For energies above ~ 10 GeV/u the fixed target mode becomes inefficient and colliding of heavy-ion beams must be used.

The first synchrotrons accelerating ions, Synchrophasotron at JINR, Bevatron at LBNL and Saturn-II at Saclay, were proton machines converted to ion synchrotrons. The first two machines were weak focusing accelerators. The upgrade included improvement of the vacuum and building of new injectors, but, in spite of these measures, only bare nuclei could be accelerated due to the poor vacuum conditions. The maximum energies were: 1.15 GeV/u for Saturn-II, 2.1 GeV/u for Bevatron, and 4.2 GeV/u for Synchrophasotron. All the three machines are already out of operation.

After the successful demonstration that heavy ions could be accelerated in proton synchrotrons BNL's AGS and CERN's SPS, ambitious heavy-ion programmes started. At BNL the emphasis was on the acceleration of gold ions up to 9 GeV/u. At CERN the so-called lead programme was initiated. The intensity of the accelerated in SPS up to 17.7 GeV/u fully stripped lead ions reached $4.7 \cdot 10^9$ ions/pulse.

Two synchrotrons specially built for heavy-ion acceleration took the baton — SIS-18 at GSI and Nuclotron at JINR. SIS-18 accelerates all ion species up to U^{73+} to a maximum energy of 1 GeV/u and with beam intensity as high as $4 \cdot 10^{10}$ ions/pulse. Nuclotron is a superconducting machine capable to accelerate ions with $Z_{\rm pr}/A_{\rm pr} = 0.5$ up to 6 GeV/u.

The story of investigations with relativistic heavy-ion beams turned over a new leaf with the commissioning of the heavy-ion collider RHIC at BNL. Collisions of gold nuclei at the maximum energy of $2 \cdot 100$ GeV/u with a peak luminosity $L = 1.5 \cdot 10^{27}$ cm$^{-2} \cdot$ s^{-1} were realized.

Principles applied for acceleration of heavy ions are the same as those applied for acceleration of protons. The breakthroughs are related mainly with the invention of the EBIS and ECRIS sources of intensive beams of heavy ions in high-charge states, with the invention of RFG accelerator and the progress made in linear injectors and with the invention of electron cooling.

The remaining bound electrons in the multielectron ions and the high electric charge of the fully stripped (bare) nuclei are the two major factors in which the acceleration of heavy ions differs from the acceleration of protons.

The multicharged ions interact with the molecules and atoms of the residual gas in the vacuum chamber of the accelerator and/or with deliberately set stripping targets. This interactions lead to loss and capture of electrons from/to the projectile electron shell and hence to a jump of the projectile charge-to-mass ratio. The ion cannot be further guided and focused by the accelerator magnetic structure in a proper way and is lost.

On the other hand, ion loss can produce vacuum pressure instability and pressure bumps, which in turn lead to more beam loss. A positive feedback could be established, and the beam could be completely destroyed.

The high electric charge $eZ_{\rm pr}$ of the fully stripped nuclei compared with the proton charge has many positive and negative consequences. Here are some of them.

• As the particle charge grows up, the influence of the adverse space charge effects also increases. The coherent space charge tune shift is proportional to $Z^2_{\rm pr}/A_{\rm pr}$. High space charge tune shift ($\Delta Q > 0.25$) results in resonance crossing and in beam loss. The intensity limitations are most severe in the booster synchrotron due to the low ion velocity at injection. The cure is to use a large acceptance and to fill this acceptance with particles as densely as possible. A kind of multiturn injection with stacking in both horizontal and vertical phase spaces could be applied. For a small machine like a booster synchrotron, the use of large acceptance is cost-reasonable.

• The beam rigidity $B\rho$ is inversely proportional to the ion charge. Increasing the ion charge you reduce the power necessary for acceleration to a given kinetic energy. On the other hand, the less the ion charge the higher space charge limit. Hence a compromise must be worked out.

• In heavy-ion colliders the beam lifetime is dominated by intrabeam scattering. This leads to particle loss out of the RF buckets and to an increase of the transverse beam emittances. The emittance growth reduces the luminosity. The intrabeam scattering effect scales as $Z^4_{\rm pr}/A^2_{\rm pr}$.

The paper represents a review of processes which are specific for high-energy heavy-ion acceleration and which determine to a great extent the achievable parameters and the quality of the accelerated beams.

1. VARIANTS OF A HIGH-ENERGY HEAVY-ION ACCELERATOR COMPLEX

The different variants of heavy-ion acceleration by synchrotrons are closely related to the available sources of heavy ions.

Three types of heavy-ion sources are nowadays in operation — Table 1.

1.1. Vacuum Arc Ion Sources. These are sources of ions in low charge state, $A/Z_{\rm pr} \leqslant 65$, but with high ion beam intensity, up to $0.25A/Z_{\rm pr}$ in emA. The achieved at GSI beam currents lie above the space charge limit of the RFQ

Table 1. **Sources of uranium ions**

Ion source	Charge state of delivered uranium ions, $Z_{\rm pr}$	Beam current, emA	Pulse length, μs
MEVVA–GSI	4	15	500
VENUS–LBNL	30	0.240	dc
EBIS–BNL	30	2.4	10
ESIS–JINR	90	7.2	10

section. Vacuum arc ion sources are relatively simple. They need neither gyrotron amplifiers nor superconducting magnets. The pulse length is long enough, 500 μs or more, for a kind of multiturn injection into synchrotron to be realized.

Vacuum arc ion sources are widely used at the GSI heavy-ion accelerator complex.

The multicasp ion source MUCIS is used for gaseous ions (deuterium, helium, argon, xenon, etc.) [1]. For example, Ar^{1+} beams with 38 emA current were produced.

For metal ions the Metal Vapor Vacuum Arc ion source MEVVA has been developed [2]. It provides uranium beams with typical total current of 24 emA and the fraction U^{4+} reaching a rate of 67%. The new modification of MEVVA ion source, named VARIS, can generate even more intensive uranium beams. With arc current 700 A at 30 kW and a careful tuning of the extraction system, the analyzed U^{4+} current has reached 25 emA.

1.2. Electron Cyclotron Resonance Ion Source, ECRIS. ECRIS was suggested by R. Geller. It is able to generate high current, medium charge state beams. The ion source operates at dc or long pulses ($\sim$ 200 μs) modes. The latter mode is called «afterglow» mode and delivers larger intensity. The ion sources of ECRIS type are very reliable and stable in operation. The recent improvements are related with raising the RF and the strength of the magnetic field applying a gyrotron amplifier and superconducting solenoidal and hexapole radial cusp magnetic fields.

The developed at LBNL superconducting ECRIS VENUS utilizes a commercially available 10 kW — CW, 28 GHz gyrotron amplifier and has a peak magnetic field of 4 T [3]. It can produce 240 eμA U^{30+} or 5 eμA U^{48+} beams.

1.3. Electron Beam Ion Source, EBIS. EBIS produces ion beams in the highest available charge states. The ion source was developed at JINR by E. D. Donets. For EBIS, the total extracted charge per pulse is independent of the ion species and of the ion charge state. The charge state distribution is narrow. Typically the desired charge state rate is about 20% of the total current. EBIS produces short pulses of high current and is well suited for single turn injection into synchrotrons but not for multiturn injection.

The recent advantages made at BNL have used an electron gun with 10 A electron beam current and a 0.7 m long trap [4]. A beam of Au^{32+} ions with 550 eμA in 15 μs pulses has been produced. BNL EBIS could also deliver beams of U^{30+} ions with intensity $5 \cdot 10^9$ ions in 10 μs pulses. The time between the successive pulses is 100 ms. This source uses a 5 T superconducting solenoid.

By using electron reflectors, E. D. Donets succeeded in formation of electron strings with high linear electron space charge density which could be used for effective production of highly charged ion beams. They called this modification of EBIS — Electron String Ion Source, ESIS [5]. In the first tests with JINR «Krion-2», converted to ESIS-type ion source, Ar^{16+} beams with current up to 150 eμA in 8 μs pulses have been produced.

1.4. Laser Ion Source, LIS. Laser ion source is also worth mentioning. It delivers short (few μs) intense ion pulses, well suited for single turn injection intosynchrotrons. A CO_2 laser is usually applied. Recently a collaboration between ITEP and TRINITI from Russia and CERN succeeded in generating of Pb^{27+} ion beams with total extracted current of 20 emA, a pulse width of several μs and repetition rate 1 Hz. A 100 J, 15–30 ns CO_2 laser was used in this LIS.

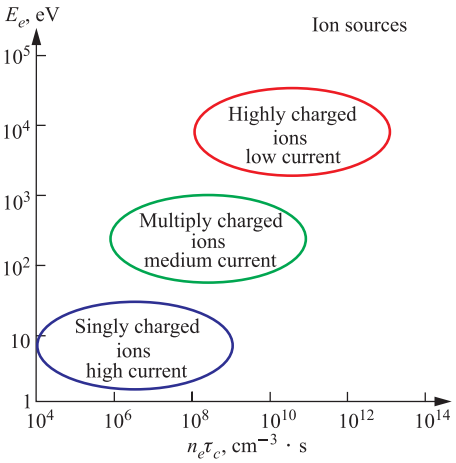

Fig. 1. Different types of ion sources. On the horizontal axis the product of electron density and confinement time is shown. On the vertical axis the electron energy is shown

To sum up — from the point of view of injection and acceleration in synchrotrons we could distinguish three groups of ion sources (Fig. 1):

— sources of single charged ions or of ions in very low charge state, but with the highest intensity, which is reached by now;

— sources of medium charged ions with medium beam current;

— sources for ions in the highest charge states, which are reached by now, but with low beam current.

The layout of the heavy-ion accelerator complex strongly depends also on the choice of the injection method. All existing methods for single and multiturn injection have been used to store ions in heavy-ion synchrotrons. From these methods only the stripping injection is specific for heavy ions.

Charge exchange injection is now the preferred injection method for proton synchrotrons due to its relative simplicity and the very high intensity of the stored beams. The charge injection in the proton machines is based on the stripping

of two electrons from H^- ions when passing through a solid foil. The stripping converts H^- ions to protons H^+. The protons move afterwards along the injection orbit. Usually a local closed orbit bump is realized during the injection period to prevent the foil crossing by the circulating beam (Fig. 2).

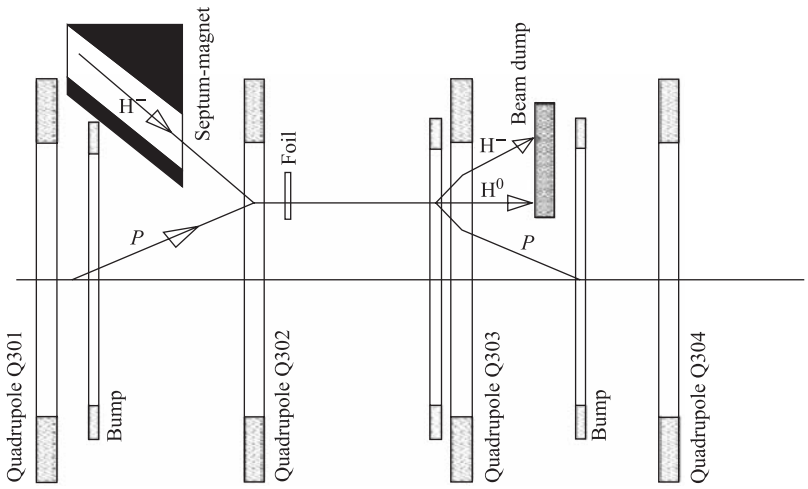

Fig. 2. H^- injection from the 8 GeV linac into the main injector in the FNAL accelerator complex

The transverse emittance growth due to the multiple Coulomb scattering in the stripping foil is the major process that limits the stored intensity.

Stripping of the remaining in multicharged ions electrons could be used for injection of heavy-ion beams. In order to strip all the electrons up to a bare nucleus the projectile must be accelerated to sufficiently high energy — the heavier ion the higher energy.

An important point in charge exchange injection of heavy ions is that the change of the ion charge state from $Z_{\rm in}$ for the injected ions to $Z_{\rm pr}$ for the circulating ions must be as high as possible. Only in this case the trajectories of injected and circulating particles have enough separation in the merging device, which could be a structural magnet or a bump magnet. For H^- injection, ion charge state jumps from -1 to $+1$ in target crossing and the merging devise bends the injected and the circulating particles in opposite directions. This is the optimum case and together with the fact that the additional electron in the H^- ion is loosely bound explains why the H^- charge exchange injection is so popular.

Fortunately, with the increase of the particle energy, the spectrum of charge states behind the stripping target becomes narrower. This results in higher rate of fully stripped ions (80% or more) and hence in more efficient injection.

One must create the necessary conditions so that the already stored and circulating in the machine ions will cross the stripping target only few times. If the transverse emittanses of the injected beam are much smaller than the accelerator acceptances, a kind of beam painting could be realized. Several schemes for beam painting have been proposed. These include: horizontal painting and vertical steering of the target, painting in both horizontal and vertical planes with correlated or anticorrelated closed orbit bumps and painting in all three directions (Fig. 3).

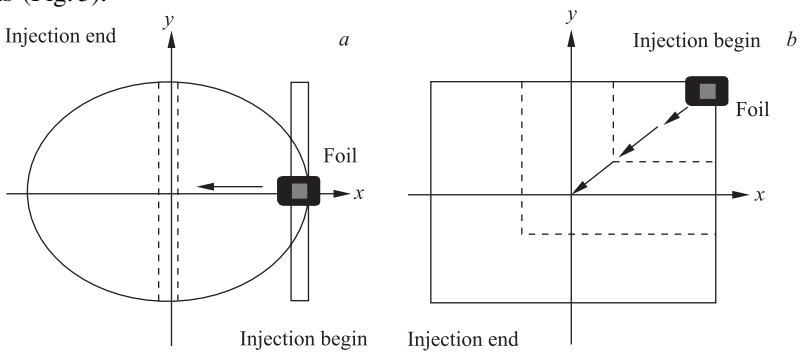

Fig. 3. Painting schemes. *a*) Horizontal orbit bump and vertical steering of the target; *b*) painting in both horizontal and vertical planes with correlated closed orbit bump

Painting can reduce the foil hits to 5–7.

The increase of the injection energy expands the range of ion species that can be injected via stripping toward the heavier ions. This also reduces the emittance growth due to the multiple Coulomb scattering as the rms scattering angle is inversely proportional to the square of projectile energy.

For injection of heavy ions, the ionization loss of energy could be a problem as the stopping force $-dE/dx$ is proportional to square of projectile charge state $Z_{\rm pr}$. On the other hand, the equilibrium thickness of the stripping target is inversely proportional to the sum of electron loss and capture cross sections. For high projectile energy the capture prevails. The electron capture cross section is inversely proportional to the square of projectile velocity. Summarizing, at high projectile velocity the overall loss of energy in target crossing is approximately independent of the particle energy. The relative change of energy, which is of importance, of course decreases.

The cooler storage ring CELSIUS in TSL was the first accelerator in which the charge exchange injection of light ions has been realized [6]. The magnetic rigidity of the storage ring is $B_0\rho = 7$ T$\cdot$m. CELSIUS can accelerate ions with charge-to-mass ratio equal to 0.5 up to 470 MeV/u. A cyclotron equipped with an ECR ion source is used as injector. It accelerates ions with $Z/A = 0.5$ up to 48 MeV/u. One of the ring dipoles serves as a merging device. A carbon foil

with a thickness of 30 μg/cm^2 is used to strip the injected ions to bare nuclei. Two bump magnets move the closed orbit locally close to the stripper. During the injection this local orbit bump exponentially falls to the machine center with a time constant in the range 4 μs–4 ms.

Protons, deuterons, alpha-particles, and light ions have been stored by means of stripping injection. For example, O_{16}^{5+} ions have been fully stripped to O_{16}^{8+}. With 1.5 μA injected current up to 150 μA, O_{16}^{8+} ions have been stored in the ring.

Three different approaches to the high-energy heavy-ion accelerator complex layout are related to the chosen ion source type and injection method.

1.5. Variant with a High Current, Low Charge State Injector. This approach to the heavy-ion acceleration has been developed for many years at GSI [7, 8]. A multicasp ion source for gaseous ions and a metal vapor vacuum arc ion source for metal ions are used. These sources deliver intensive beams of low charged ions.

The first section of the GSI high current linear injector is a 36 MHz, 9.4 m long, RFQ structure, working in H_{110} mode [9]. This first section accelerates ions up to 120 keV/u. It is followed by a 20 m long IH drift tube linac. This IH-DTL further accelerates ions to 1.4 MeV/u, an energy that is high enough for a N_2-jet stripper to be applied. The gas stripper raises the ion charge state from U^{4+} to U^{28+}. Energy of 1.4 MeV/u is too low and the stripping efficiency is only 12%. This is compensated by the high intensity of the source (15 emA for U^{4+}).

The famous UNILAC then takes the baton. It pushes ions up to 11.4 MeV/u. At this energy a C-foil stripper can be applied. This second stripper raises the ion charge from U^{28+} to U^{73+}. The reported stripping efficiency is 15%. Energy of 11.4 MeV/u is high enough to guarantee small residual gas loss in the SIS-18 synchrotron.

We could generalize the GSI approach in the following way (Fig. 4).

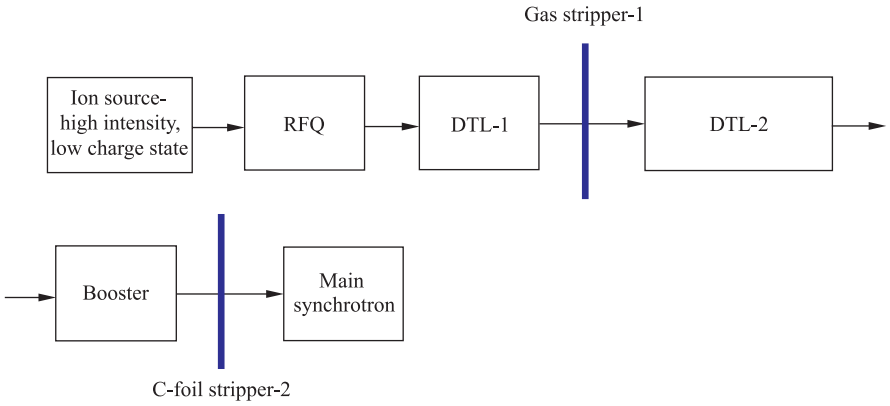

Fig. 4. Variant with a high current, low charge state injector

The basic idea is the use of an intensive source of ions in low-charge state. Acceleration of low-charged ions by linear accelerators requires high accelerating voltage, and as the voltage gain is limited (4.2 MV/m in the GSI IH-DTL), the length of the linac becomes large. The linear injector must be split to two parts with a stripping section between them. In this way you increase the ion charge state at as low energy as possible. Large particle loss due to the bad stripping efficiency at low projectile energy is the price you must pay.

As the pulse length of the used ion sources is large (500–1000 μs) a multiturn injection into the booster synchrotron with big number of injected turns could be realized.

1.6. Variant with Source of Heavy Ions in Medium Charge States, Working in dc Mode. The only source of multicharged ions working in dc mode at the moment is ECRIS. The beam current of the state-of-art ion sources of this type is 200–400 eμA depending on the ion species and could be doubled in the pulse (afterglow) mode with 200–300 μs pulses. This approach to heavy-ion acceleration is realized in the LHC lead acceleration chain [10, 11]. CERN's ECRIS works at 14 GHz and produces beams of Pb^{27+} ions with 200 eμA beam current.

The much higher charge states of the ions delivered by ECRIS compared with those from vacuum arc ion source allow one to drop out the first stripper in Fig. 4 and thus to increase the efficiency almost ten times, Fig. 5.

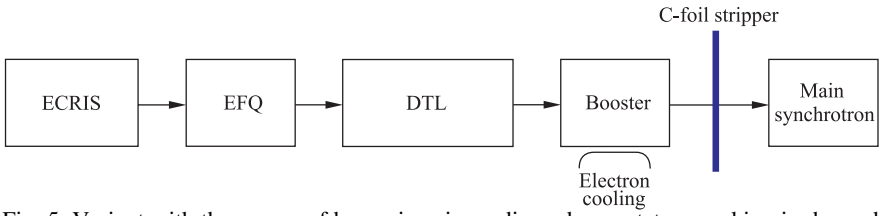

Fig. 5. Variant with the source of heavy ions in medium charge states, working in dc mode

On the other hand, the dc nature of ECRIS allows applying efficient multiturn injection into the booster synchrotron. In CERN Pb programme the injection in LEIR covers 35 turns, with 25 effective ones. An original method for combined injection in both transverse and longitudinal phase spaces is used. This method increases the stored intensity 3 to 5 times and simultaneously reduces the beam emittance 3 times. After the multiturn injection is fulfilled, the stored beam is cooled down applying the electron cooling method. The cooling time is short — 0.1 s. This allows for up to 12 stacking – cooling cycles to be realized.

1.7. Variant with Injector of Heavy Ions in High Charge States, Working in a Short Pulses Mode. The ion source that delivers heavy ions in the highest at the moment charge states is EBIS. EBIS is able to produce highly charged ions of any species. It has the smallest beam emittance.

With ions in high charge states the RFQ and DTL sections are more compact and efficient.

EBIS is a pulsed ion source. The pulses of extracted ions are short, typically about 10 μs. The pulse length is of the order of the booster revolution time, and the single turn injection is the natural choice. The repetition rate of EBIS is 1–5 Hz. In principle, one could repeat the single turn injection several times stacking the particles in the momentum space.

The accelerator chain is schematically shown in Fig. 6.

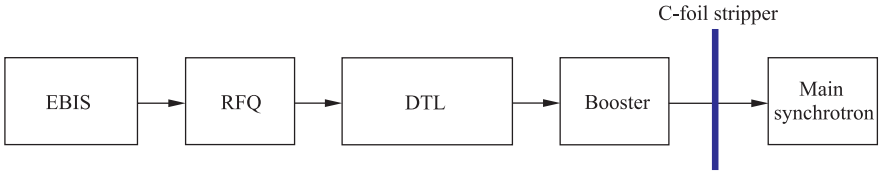

Fig. 6. Variant with injector of heavy ions in high charge states, working in a short pulses mode

This approach has been applied to the JINR Synchrophasotron and after its shutdown to the Synchrophasotron's successor — the superconducting heavy ion synchrotron Nuclotron [12]. The developed by E. D. Donets EBIS «Krion-2» can produce, for example, 8 μs pulses of Ar^{16+} and Fe^{24+} ions with beam currents of 200 and 150 eμA, respectively. The repetition rate is 1 Hz.

An important step toward higher beam intensity was made recently at BNL. Increasing the electron current in a test EBIS up to 10 A and improving the ion confinement, the BNL team succeeded in producing Au^{35+} beams with $3 \cdot 10^9$ ions/pulse. This success encouraged the BNL specialists and they have proposed to replace the Tandem injector with a combination of EBIS, RFQ and short linac [13].

Meanwhile, E. D. Donets started at JINR R&D investigations in a completely new direction. He suggested the so-called reflex mode of EBIS operation. The new source was named Electron String Ion Source or ESIS. The hopes are that with a 12 T superconucting solenoid this source will be able to produce beams of ions with mass number A from 130 to 238, in high charge state $Z_{\rm pr}$ from 0.42 to 0.38, and with high intensity $N = 1 \cdot 10^{10} - 5 \cdot 10^9$ ions/pulse. Plans to use ESIS in the injection chain are under way [14].

2. INTERACTION WITH RESIDUAL GAS AND STRIPPING FOILS

When the ion beam moves in the accelerator, the multielectron ions interact with atoms and molecules of the residual gas or with those in solid or gaseous targets, deliberately introduced in their path. These interactions include elastic and inelastic processes: single and multiple Coulomb scattering, processes of

electron loss and capture, and processes of excitation and ionization of target atoms and molecules. The loss or capture of electrons by fast moving ions results in the change of ion charge and hence leads to beam loss. The multiple Coulomb scattering has, as a consequence, an increase of transverse emittance. Spending of ion kinetic energy for excitation and ionization of target atoms increases the relative momentum spread.

In this chapter, a brief description of all these processes is given.

2.1. Electron Loss. This is a process of loss of electrons in ion-atomic collisions — Fig. 7. The figure of merit is the so-called atomic velocity $v_0 = e^2/\hbar = \alpha\, c = 2.19 \cdot 10^6$ m/s, where $\alpha = 1/137$ is the fine structure constant. In fact, v_0 is the velocity of an electron in the first Bohr orbit.

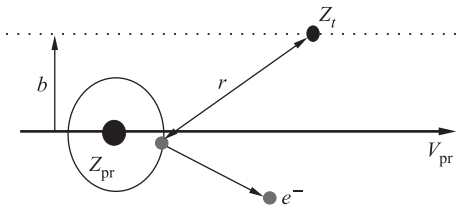

Fig. 7. Process of single electron loss in ion-atomic collisions

According to the Bohr criterion when an ion penetrates through matter, it retains only those electrons whose orbital velocity u is greater than the ion velocity $v = \beta c$. For hydrogen-like particles with charge of the nuclei $eZ_{\rm pr}$, the mean electron orbital velocity is $u = Z_{\rm pr}\, v_0$. For such a hydrogen-like ion the electron loss cross section has a maximum for $v = u$.

When the ionization is due to atoms instead of nuclei, the screening of the nuclear charge by the shell electrons leads to smaller ionization cross section.

Let $\sigma_{i,i+1}$ be the cross section for the loss of single electron by a multielectron ion being in charge state i.

The classical Bohr formula [15] predicts:

$$\sigma_{i,i+1} = 4\pi a_0^2 \frac{Z_t^2 + Z_t}{Z_{\rm pr}^2} \left(\frac{v_0}{v}\right)^2, \tag{1}$$

where $Z_{\rm pr}$ is ion atomic number; Z_t — target atomic number; v_0 — atomic velocity unit, $a_0 = \hbar^2/m_e c^2 = 0.529 \cdot 10^{-10}$ m — radius of the first Bohr electron orbit.

This formula is valid for projectile kinetic energy per atomic mass unit T_n, which satisfies the condition:

$$T_n > 0.05 Z_{\rm pr}^2 \text{ MeV/u}, \tag{2}$$

and for Z_t not much larger than $Z_{\rm pr}$. For uranium ions the condition (2) reads: $T_n > 420$ MeV/u.

V. S. Nikolaev et al. [16] have introduced the following correction factor to the Bohr formula:

$$\left[D - \left(\frac{Z_{\rm pr} v_0}{2v}\right)^2\right], \tag{3}$$

where

$$\begin{gathered} D = \frac{Z_{\rm pr}^2}{2Z_t^2} \quad \text{for} \quad \frac{Z_{\rm pr}}{Z_t} < \frac{3}{4}, \qquad D = \frac{3Z_{\rm pr}}{8Z_t} \quad \text{for} \quad \frac{3}{4} \leqslant \frac{Z_{\rm pr}}{Z_t} \leqslant 4, \\ D = 1 + 0.56 \ln\left\{\min\left[\left(\frac{1.6v}{Z_{\rm pr} v_0}\right), \left(\frac{Z_{\rm pr}}{2Z_t}\right)\right]\right\} \quad \text{for} \quad \frac{Z_{\rm pr}}{Z_t} > 4. \end{gathered} \tag{4}$$

This formula is valid for $T_n > 0.1 Z_{\rm pr}^2$ MeV/u for particles with $Z_{\rm pr} < Z_t/\sqrt{2}$ and for $T_n > 0.2 Z_{\rm pr}^2$ MeV/u for ions with $Z_{\rm pr} > Z_t/\sqrt{2}$.

There is no satisfactory quantitative theoretical description of the electron loss and capture cross sections. These cross sections depend sharply on the projectile velocity, as well as on the atomic numbers of the projectile and target atoms and on ion charge state i. Also there is a lack of sufficient amount of experimental data on ionization cross sections for high-energy highly charged states heavy ions.

Most reliable approach to estimate the cross sections is the direct measurement. However, it is difficult to measure cross sections before the accelerator is built because you need ion species at the specified energy range. The available data are for the energies reached in heavy ion cyclotrons and at GSI and BNL accelerator complexes.

Analyzing the experimental data, B. Franzke has proposed a semiempirical formula for the electron loss cross section by fast ions [17], which received big popularity:

$$\sigma_{i,i+1} = 3.5 \cdot 10^{-18+(0.71 \lg Z_{\rm pr})^{3/2}} \frac{\bar{q}_t}{\bar{q}_{\rm pr}\sqrt{\gamma^2 - 1}} \left(\frac{q_{\rm pr}}{\bar{q}_{\rm pr}}\right)^{-4}, \tag{5}$$

where $\bar{q}_{\rm pr}$ and $\bar{q}_t$ are the equilibrium charge states of the projectile and target ions; and γ and β are the relativistic factors. For the equilibrium charge, Franzke used the formula:

$$\bar{q} = Z\left(1 - \exp\left(-\frac{137\beta}{Z^{0.67}}\right)\right). \tag{6}$$

A comparison between the experimental data and the Franzke formula is given in Fig. 8 for 4.66 MeV/u Pb^{54+} and in Table 2 for 3.5 and 6.5 MeV/u U^{28+} ions.

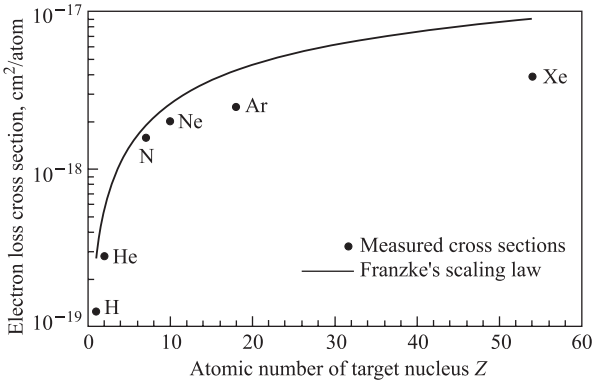

Fig. 8. Electron loss cross section for Pb^{54+} ions at 4.66 MeV/u. The dots are the experimental results and the solid line is the result obtained by the Franzke formula [18]

Table 2. **Comparison of the experimental cross sections and the Franzke formula. The cross sections are in 10^{-18} cm^2/atom [19]**

U^{28+}	Target	Experiment	Franzke
3.5 MeV/u	H_2	1.62	4.0
	N_2	22.52	26.9
	Ar	45.38	58.9
6.5 MeV/u	H_2	1.14	0.85
	N_2	14.69	5.89
	Ar	33.15	13.80

2.2. Electron Capture. Several processes contribute to the electron capture:

Direct Electron Capture (DEC). DEC is relevant for fully stripped and not too heavy ions and target atoms. The process is also known as direct Coulomb capture and can be described as

$$Z_{\rm pr} + (Z_t + e) \rightarrow (Z_{\rm pr} + e) + Z_t. \tag{7}$$

The electron capture takes place mainly for projectile velocities $v = \beta c$ which are close to the orbital velocity of the target electron u. Due to this velocity, matching of the capture of K-shell target electrons into the K shell of the projectile ion prevails. In DEC, there is no photon emission. The process is important for low projectile energies. For completely stripped heavy ions in the MeV/u range the cross sections are of the order of 10^{-27} cm^2/atom.

For projectile energies T_n in MeV/u, which satisfy the conditions:

$$T_n > 0.05 Z_{\rm pr}^2 \quad \text{and} \quad T_n > 0.05 Z_t^2. \tag{8}$$

A simple approach to describe the nonradiative electron capture cross section is the Oppenheimer–Brinkmann–Kramer or OBK theory [20].

The nonradiative electron capture occurs mainly at the velocity matching condition $v_{\rm pr} \approx u, u$ being the velocity of the captured electron, bound in the target atom. For $v_{\rm pr} \gg u$:

$$\sigma_{\rm NRC} \propto \frac{Z_t^5 \, Z_{\rm pr}^5}{v^{11}}. \tag{9}$$

For high projectile energies, electronic velocity matching becomes not probable and radiative electron capture takes place.

Radiative Electron Capture (REC). REC dominates at high projectile energies when the electrons bound in the target atoms can be considered as free. The excess of energy is radiated as a photon (Fig. 9) or schematically:

$$Z_{\rm pr} + e \rightarrow (Z-1)_{\rm pr} + \hbar\omega. \tag{10}$$

A theoretical estimation of the REC cross section is given by the formula, derived by Oppenheimer [21]. Speaking qualitatively, the REC cross section grows quickly with $Z_{\rm pr}$ and decreases rapidly with the projectile velocity:

$$\sigma_{\rm REC} \propto \frac{Z_t \, Z_{\rm pr}^5}{v_{\rm pr}^5}. \tag{11}$$

REC cross sections for fully stripped uranium ions are of the order of 10^{-22} cm^2/atom. Similar to REC is the Radiative Recombination (RR), which is the process of radiative transfer of bound electron from the target atom to the projectile.

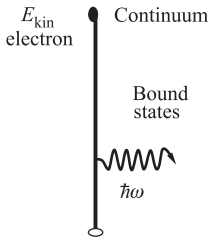

Fig. 9. Radiative Electron Capture (REC)

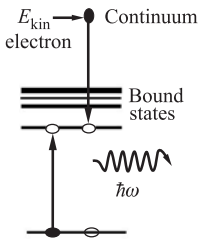

Fig. 10. Dielectronic Recombination (DER)

Dielectronic Recombination (DER). DER is a resonant process in which the excess of energy is used to excite an electron in the projectile ion (Fig. 10). DER takes place in beams of not fully stripped ions. At resonant energies, cross sections of DER can be compatible to those of REC at low velocity.

Between empirical formulae for single electron capture cross sections the best approximation gives the Schlachter scaling rule [22]. The accuracy of this empirical rule for ions from He to U and energies from 100 keV/u up to 10 MeV/u is higher by an order of magnitude. This is the reason why the Schlachter rule has gained a big popularity. This rule is expressed by the equation:

$$\tilde{\sigma}_{\mathrm{cap}} = \frac{1.1 \cdot 10^{-8}}{\tilde{E}^{4.8}} \left(1 - \mathrm{e}^{-0.037\,\tilde{E}^{2.2}}\right)\left(1 - \mathrm{e}^{-2.44 \cdot 10^{-5}\,\tilde{E}^{2.6}}\right), \tag{12}$$

where the reduced energy $\tilde{E}$ is given by

$$\tilde{E} = \frac{E}{Z_t^{1.25}\, i^{0.7}} \tag{13}$$

and the reduced capture cross section $\tilde{\sigma}_{\mathrm{cap}}$ is given by

$$\tilde{\sigma}_{\mathrm{cap}} = \frac{\sigma_{\mathrm{cap}}\, Z_t^{1.8}}{\sqrt{i}}, \tag{14}$$

i being the projectile charge state.

A comparison between the experimental data and Schlachter's empirical scaling rule for Pb^{54+} ions at 4.66 MeV is shown in Fig. 11.

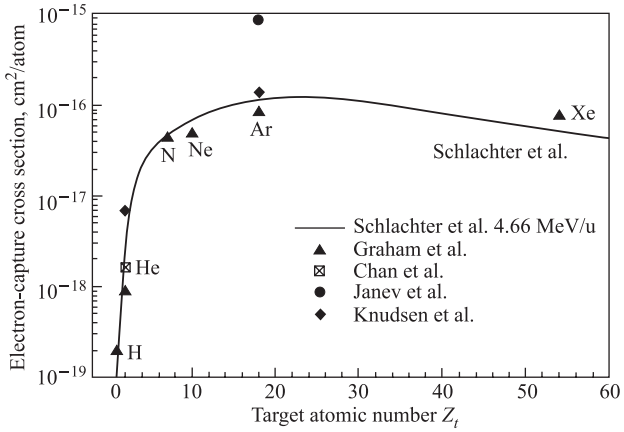

Fig. 11. Single electron capture cross section as a function of the atomic number of the target gas for 4.66 MeV Pb^{54+} ions. The solid line represents Schlachter's empirical scaling law and the points — experimental and theoretical results [18]

2.3. Interaction with the Residual Gas and Beam Lifetime. When ions collide with the residual gas atoms and molecules in the vacuum chamber of the accelerator, abrupt changes of the ion charge state lead to beam loss.

In synchrotrons, the energy gain per turn $\Delta T_{\rm turn}$ is proportional to the ratio i/A, i being the projectile ion charge state and A — the projectile mass number. The heavier ion and the lower its charge state, the slower goes acceleration. Thus for U_{238}^{10+} ions (GSI) $i/A = 0.042$; for Au_{197}^{33+} ions (BNL) $i/A = 0.167$; for Pb_{207}^{54+} ions (CERN) $i/A = 0.26$; for U_{238}^{73+} ions (GSI) $i/A = 0.30$, while for protons this ratio is equal to unit.

As a rule, the heavy ions need much more time to reach the maximum energy of the machine.

While for protons the interaction with the residual gas consists in Coulomb scattering and in excitement and ionization of atoms, for heavy ion beams the major process is the process of charge exchange.

Above 20 MeV/u the loss of electrons (stripping) prevails over the electron capture.

For synchrotrons accelerating heavy ions, the injection energy is usually much lower than the injection energy in proton machines. For low energy of the ions, however, the cross sections for charge exchange are high. Thus, for 10 MeV/u U or Pb ions the charge exchange cross section is of the order of 10^{-16} cm^2.

The standard multiturn injection with stacking in horizontal phase space takes relatively small time. For example, SIS 40-turn injection of U_{238}^{73+} at 11.4 MeV/u lasts about 200 μs. On the contrary, RF stacking in longitudinal phase space takes much more time. Thus, the RF injection into TSR storage ring in Heidelberg, which covers 25 cycles, lasts about 250 ms. In the BNL–EBIS project the injection of 4 EBIS pulses in the longitudinal phase space of the AGS booster is supposed to take about 450 ms. Hence, in the case of RF stacking the vacuum related beam loss will be much higher.

The beam lifetime is given by

$$\frac{1}{\tau} = v_{\rm pr}\, \sigma_{\rm tot}\, n, \tag{15}$$

where $\sigma_{\rm tot}$ is the total charge changing cross section in cm^2/atom and n is the gas density in atoms/cm^3.

$$n = 9.656 \cdot 10^{18}\, \frac{p}{T}, \tag{16}$$

where p is the residual gas pressure in Torr and T — absolute temperature in K.

It follows from (15), (16) that the one revolution transparency of the accelerator at 20 °C is given by

$$D = \exp\left(-3.293 \cdot 10^{16} p\, \sigma_{\rm tot}\, L\right), \tag{17}$$

where L is the accelerator circumference in cm.

We should take into account that the total charge exchange cross section $\sigma_{\rm tot}$ in (17) is a function of projectile nuclear charge $Z_{\rm pr}$, target (i.e., residual gas) nuclear charge Z_t, and projectile velocity $v_{\rm pr}$ at the specified point of the accelerator cycle, $\sigma_{\rm tot} = \sigma_{\rm tot}(Z_{\rm pr}, Z_t, v_{\rm pr})$.

In a mixture of gases, which is the case of residual gas in accelerators, the beam lifetime and the accelerator transparency are sums of the partial beam lifetimes and transparences:

$$\frac{1}{\tau_{\text{tot}}} = \frac{1}{\tau_{\text{H}_2}} + \frac{1}{\tau_{\text{CO}_2}} + \frac{1}{\tau_{\text{N}_2}} + \ldots, \quad D = D_{\text{H}_2} + D_{\text{CO}_2} + D_{\text{N}_2} + \ldots \qquad (18)$$

The lifetime of Pb^{53+} ion beam in CERN PSB is shown in Fig. 12 as a function of ion energy [23].

Vacuum induced beam loss has been measured in all the existing heavy-ion machines. As an example we will give here the results obtained in the

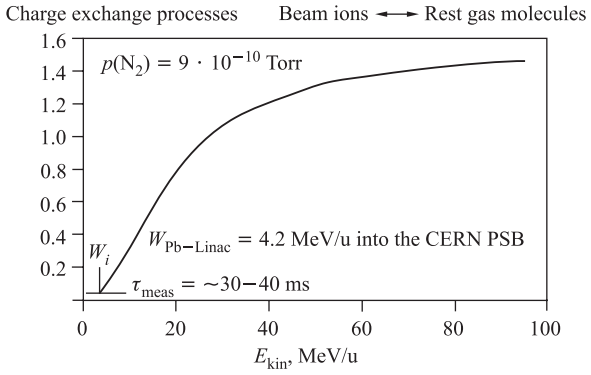

Fig. 12. Lifetime of Pb^{53+} ions in PSB [23]

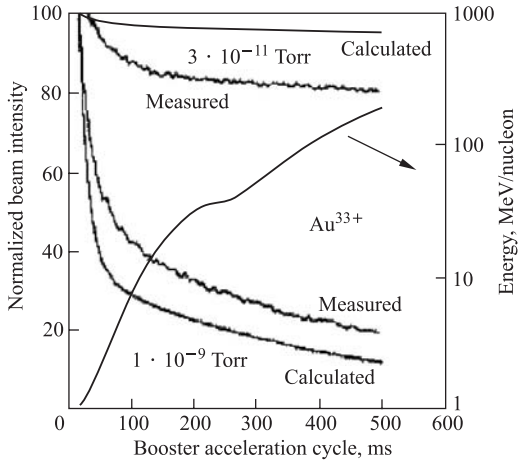

Fig. 13. The fraction of survival Au^{33+}beam during the BNL Booster cycle at vacuum levels of 10^{-9} Torr and $3 \cdot 10^{-11}$ Torr [24]

BNL Booster [24]. In this accelerator the vacuum related beam loss has been measured at two different vacuum conditions: the normal operating pressure of $3 \cdot 10^{-11}$ Torr with over 70% H_2 and for pure vacuum of $1 \cdot 10^{-9}$ Torr with 50% Ar and 35% CH_4 (Fig. 13). The beam consists of Au^{33+} ions and the acceleration cycle lasts 500 ms.

2.4. Evolution of the Ion Charge State; Equilibrium Charge State Spectrum. As the cross sections for loss and capture of one electron are much larger than the cross sections for loss and capture of two and more electrons, the process of change of the initial ion charge i_0 to the final spectrum of charges $i_1, i_2, \ldots$, is a process of gradual change of the ion charge (Fig. 14).

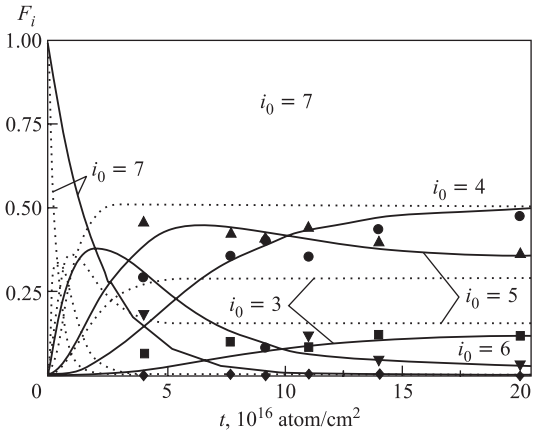

Fig. 14. Evolution of charge state spectrum with the target thickness. Data are for nitrogen ions with initial velocity $v = 3.6v_0$. Solid lines are for celluloid foil, dashed lines — for gaseous nitrogen targets [25]

One must take into account that the electron capture cross sections are much less than the electron loss cross sections. For $Z_{\rm pr} \geqslant 7$ and $E_{\rm pr} \geqslant 0.1 Z_{\rm pr}^2$ MeV/u we can find that

$$\sigma_{Z,Z-1} \leqslant \frac{1}{8}\,\sigma_{Z-1,Z}. \tag{19}$$

Going deeper and deeper in the target, the mean charge of the ion beam is approaching fluently its equilibrium value (Fig. 15).

Let $\Phi_i(t)$ be the yield of ions in charge state i, after traversing a target with thickness t, atom/cm^2, so that $\Phi_i(0)$ represents the initial distribution of ions on charge states.

For a monochromatic beam penetrating through matter, the change in the charge state distribution is described by the following set of ordinary differential

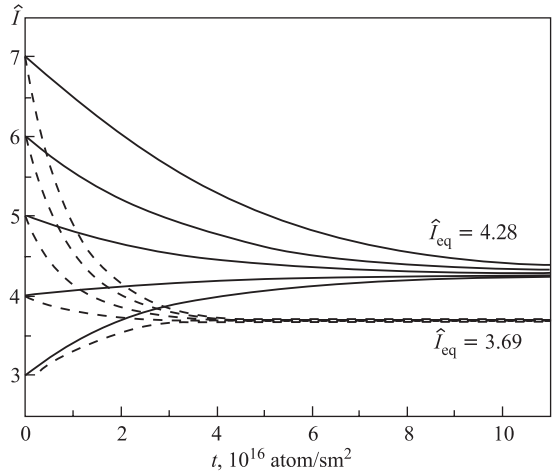

Fig. 15. Evolution of mean charge with the target thickness. The data are for nitrogen ions with initial velocity $v = 3.6v_0$. Solid lines are for celluloid foils, dashed lines — for gaseous nitrogen targets [25]

equations [26]:

$$\frac{d\Phi_i}{dt} = \sum_k \Phi_k \sigma_{ki} - \Phi_i \sum_k \sigma_{ik}, \quad i = 1, 2, \ldots, N, \tag{20}$$

where σ_{ik}, with $i \neq k$, is the total cross section for changing of the ion charge from the initial value i to the final value k, due to the processes of electron capture and loss.

As the target thickness t increases, the charge state spectrum $\Phi_i(t)$ changes quickly toward an equilibrium charge state distribution F_i, which does not depend on the target thickness t and on the initial distribution of ions on charge states $\Phi_i(0)$. The equilibrium thickness $t_{\rm eq}$ depends only on the projectile velocity $v_{\rm pr}$ and on the nuclear charge $Z_{\rm pr}$ of the projectile ions and on the target species Z_t.

The equilibrium charge state spectrum F_i is a solution of the following system of algebraic equations:

$$\sum_k F_k \sigma_{ki} - F_i \sum_k \sigma_{ik} = 0, \quad i = 1, 2, \ldots, N. \tag{21}$$

The equilibrium charge state spectrum is determined by the relations between the electron loss and capture cross sections at the specified beam energy. For the applications it is important that it does not depend on the initial ion beam charge i_0.

The equilibrium thickness $t_{\rm eq}$ increases slowly with $v_{\rm pr}$.

Along with the charge state distribution, the mean charge $\bar{i}$ and the width of the distribution or standard deviation d tend to equilibrium.

If $\bar{i}$ is not too close to 0 or $Z_{\rm pr}$, the equilibrium charge state distribution F_i can be approximated by a Gaussian:

$$F_i = \frac{1}{\sqrt{2\pi d^2}} \exp\left[-\frac{(i-\bar{i})^2}{2d^2}\right]. \tag{22}$$

This distribution has two parameters: equilibrium mean charge $\bar{i}$ and equilibrium standard deviation d.

H. H. Beckman and H. D. Betz [27] have proposed a semiempirical formula for $\bar{i}$, which gives good results for gaseous strippers and for $\bar{i}/Z_{\rm pr} > 0.3$, i.e., for high projectile energies:

$$\bar{i} = Z_{\rm pr}\left[1 - \exp\left(-\frac{v}{v_0\, Z_{\rm pr}^{2/3}}\right)\right]. \tag{23}$$

In solids the atomic density is much higher than in gases. Hence, in solids the time between two successive collisions of the projectile becomes shorter than the excited level lifetime and the excited ion fails to decay to its ground state before the next collision to occur. Moreover, due to the small interatomic distance in solids the excited states of the ion with high principal quantum number n are not allowed. These circumstances lead to an increase of the mean charge and of the equilibrium thickness in solid foils compared with gaseous targets (Fig. 16).

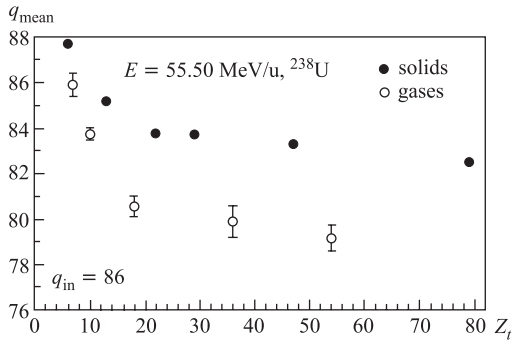

Fig. 16. Mean charge states of U^{86+} ions at 55.50 MeV/u passing through gaseous and solids as a function of the target atomic number Z_t [28]

According to measurements [29], the projectile energies necessary to reach 80% yield of bare ions in passing through Al foils are: 570 MeV/u for Au and 1.1 GeV/u for U species (Fig. 17). The equilibrium thicknesses of the Al foil are

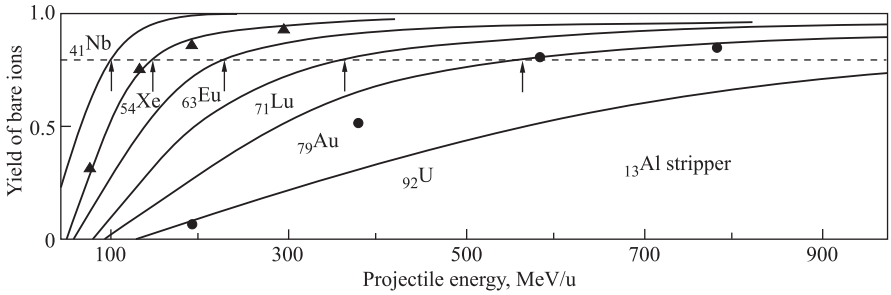

Fig. 17. Fractional yields of bare ions in Al foil as a function of projectile energy (the dashed line indicates 80% yield level) [29]

210 and 360 mg/cm^2, respectively. Half of these thicknesses will still provide 65–70% bare ions.

V. S. Nikolaev and I. S. Dmitriev [30] have proposed a semiempirical formula for mean charge in solid strippers:

$$\bar{i} = Z_{\rm pr}\left[1+\left(\frac{v}{v'\,Z_{\rm pr}^{0.45}}\right)^{-1.67}\right]^{-0.6}, \tag{24}$$

where $v\prime = 3.6\cdot 10^8$ cm/s.

For standard deviation V. S. Nikolaev and I. S. Dmitriev [30] have proposed the expression:

$$d = 0.5\sqrt{\bar{i}\left(1-\left(\frac{\bar{i}}{Z_{\rm pr}}\right)^{1.67}\right)}. \tag{25}$$

For sufficiently high ion energies only two charge state fractions Φ_{z-1} and Φ_Z prevail and should be taken into account. Experiments show that for projectile energies greater than $T_n \geqslant 0.17Z_{\rm pr}^2$ the contribution of all the charge state fractions other than Z and $(Z-1)$ is less than 3%. For this particular case the solution of (17) is:

$$\Phi_i(t) = F_i + \Delta\Phi_i\,{\rm e}^{-\kappa t}, \tag{26}$$

where $\Delta\Phi_i = \Phi_i(0) - F_i$ and $\kappa = \sigma_{Z-1,\,Z} + \sigma_{Z,\,Z-1}$.

It can be found from (26) that the equilibrium thickness (with 99% accuracy) is given by the formula:

$$t_{\rm eq} = \frac{4.6}{\sigma_{Z-1,\,Z} + \sigma_{Z,\,Z-1}}\ [{\rm atom/cm^2}]. \tag{27}$$

Stripping of fast moving heavy ions is widely used in accelerator practice both for charge exchange injection [6] or to increase the charge of the ions for their further acceleration [31]. The latter option is traditional for the heavy-ion accelerator complexes.

In BNL accelerator complex, the Au^{33+} ion beam accelerated in the Booster to kinetic energy of 192 MeV/u passes later through a 56 mg/cm^2 thick carbon stripping foil to be stripped to Au^{77+}. The thickness of the carbon foil was chosen to give the maximum yield of Au^{77+} ions. The space charge spectrum after the stripping is shown in Fig. 18. The maximum Au^{77+} ion yield is 65%.

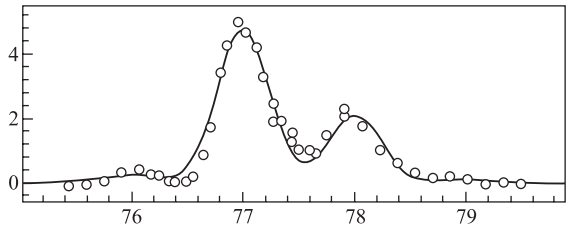

Fig. 18. Charge state spectrum of Au^{33+} ions at 192 MeV/u stripped by a 56 mg/cm^2 carbon foil [31]

For producing of fully stripped uranium an energy of at least 500 MeV/u is required.

The equilibrium charge state spectra of uranium projectiles behind Ta and Cu foils at two energies, 437 and 962 MeV/u, are represented in Table 3.

Table 3. **The equilibrium charge state spectra of uranium projectiles behind Ta and Cu foils at 437 and 962 MeV/u**

Stripping foil	Charge state spectrum at 437 MeV/u			Charge state spectrum at 962 MeV/u	
	90+	91+	92+	91+	92+
Ta, 85 mg/cm^2	25	50	30	10	90
Cu, 150 mg/cm^2	15	40	45	15	85

Equilibrium charge state spectra of U ions penetrating C foils, as they have been measured in the GSI accelerator complex, are shown in Fig. 19. The left spectrum was measured at the UNILAC behind a 40 μg/cm^2 thick target for energy of 1.4 MeV/u. The distribution depicted in the middle of Fig. 19 was obtained behind a 490 μg/cm^2 target and at the energy of 11.4 MeV/u. The spectrum displayed on the right was measured at SIS-18 synchrotron behind a 400 mg/cm^2 target at 940 MeV/u.

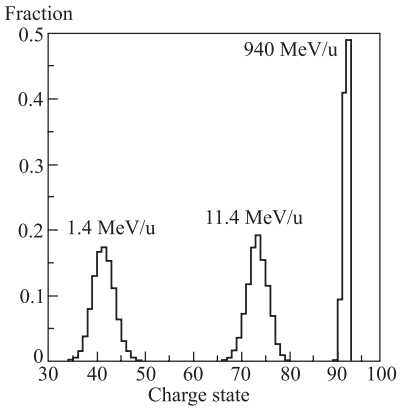

Fig. 19. Equilibrium charge state spectra of U projectiles behind C foils

2.5. Energy Loss. The mean energy loss due to excitation and ionization of the target atoms is well described by the Bethe–Bloch equation [32]:

$$\frac{dE}{dt} = -\frac{0.3070 Z_t}{A_t}\left(\frac{Z_{\rm pr}}{\beta_{\rm pr}}\right)^2 \ln\left(\frac{2m_e c^2 \beta_{\rm pr}^2 \gamma_{\rm pr}^2}{\bar{I}}\right) \ [\mathrm{MeV}/(\mathrm{g/cm}^2)], \qquad (28)$$

where t is the target thickness in g/cm^2; m_e — the electron mass; $\beta_{\rm pr}$, $\gamma_{\rm pr}$ — the projectile reduced velocity and energy (relativistic factors), and $\bar{I} \approx 13.6\, Z_t$ eV is the mean ionization potential of the target atoms.

The energy loss straggling is small and could be neglected in most cases. But it must be taken into account in some specific circumstances. One such case is when the energy loss in single internal/stripping target crossing is comparable with the momentum acceptance of the machine.

The statistical distribution of ionization losses is governed by the Landau, Vavilov or Gaussian distribution functions depending on the projectile charge and velocity. There exist standard computer subroutines that calculate these functions, for example, in the CERN computer code library.

The ionization loss of energy plays an important role in the charge exchange injection as it increases the relative momentum spread. The value of the momentum spread is determined by the spread in the number of stripping foil traversals and by the velocity and species of the injected ions.

Measured energy loss of U^{86+} ions at 60.23 MeV/u behind Al foil is shown in Fig. 20 [28].

The real phenomenon is more complicated, as starting from the initial charge state the charge content of the beam evolves gradually to equilibrium charge distribution as the particles penetrate in the foil. More precise theoretical re-

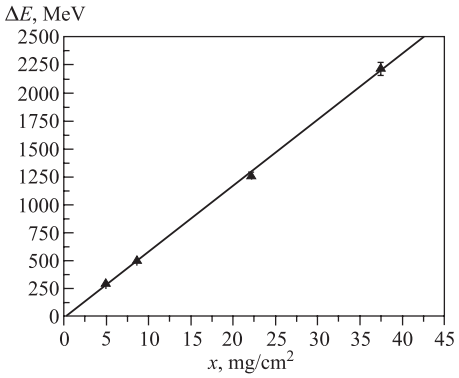

Fig. 20. Measured energy loss vs. target thickness of an incident U^{86+} beam at 60.23 MeV/u penetrating aluminum foils of various thicknesses. The data are fitted with a straight line [28]

sults about the stripping force can be obtained by the simulating computer codes GLOBAL [28] and ETACHA [33]. For a comparison between theoretical predictions and measurements, we will present here the data obtained for U^{86+} ions at 58.74 MeV/u behind a C foil. While the theoretical stopping force is: $-dE/dx = 65.69$ MeV/(mg/cm^2), the measurements point out the value: $-dE/dx = 66.50$ MeV/(mg/cm^2).

2.6. Elastic Scattering. The multiple Coulomb scattering of the projectile ions in the stripping foil or in the molecules of the residual gas in the accelerator vacuum chamber causes changes of the trajectory slope and hence transverse emittance growth. The transverse emittance growth when a beam of relativistic ions crosses a solid foil many times is one of the major limiting factors for the charge exchange injection of protons and heavy ions. Multiple Coulomb scattering in residual gas molecules also must be taken into account especially in heavy ion storage rings and colliders.

The following empirical formula can be used for mean square scattering angle of heavy ions passing through solid foils [34]:

$$\langle\theta^2\rangle = 0.250\,\frac{Z_t\,(Z_t+1)}{A_t}\,\frac{Z_{\rm pr}^2}{E_{\rm pr}^2}t, \tag{29}$$

where θ is in mrad, the stripper thickness t is in μg/cm^2, and the projectile energy $E_{\rm pr}$ is in MeV.

A useful expression for the speed of the scattering angle increase when ions interact with the molecules of the residual gas is given by B. Franzke [35]:

$$\frac{d\langle\theta^2\rangle}{dt} = 4.8 \cdot 10^{-4} P \left[m_t Z_t^2 \ln\left(\frac{204}{Z_t^{1/3}}\right)\right] \left(\frac{Z_{\rm pr}}{A_{\rm pr}}\right)^2 \frac{1}{\beta_{\rm pr}^3 \gamma_{\rm pr}^2}, \qquad (30)$$

where m_t is the number of atoms per molecule and P is the residual gas pressure in mbar. The formula is valid for room temperature. The speed of scattering angle increase is in rad/s. The values of the «target factor», given in the square brackets, are presented in Table 4 for molecules that are typical for a UHV system.

Table 4. **Values of «target factor» in Franzke's formula for the speed of scattering angle increase in ion interactions with the residual gas**

Molecule	$m_t Z_t^2 \ln(204/Z_t^{1/3})$
H_2	10.6
He	20.3
Ne	455
N_2	485
CO	466
O_2	592
CO_2	762
Ar	1411

From Table 4 it becomes obvious that the fraction of heavy atoms in the residual gas must be as small as possible.

The change of the transverse RMS emittance which is caused by the elastic scattering is given by [36]:

$$\varepsilon_N = \varepsilon_0 + 2N\beta^*\langle\theta^2\rangle, \qquad (31)$$

where ε_0 is the initial emittance; β^* is the value of the amplitude function at the foil and N is the number of foil passages.

If the dispersion at the stripper is nonzero, the ionization loss of energy, described in the previous point, also will cause transverse emittance growth. This kind of emittance growth could be evaluated by the formula:

$$\sqrt{\beta^*\varepsilon} = \sqrt{\beta^*\varepsilon_0} + N\sqrt{(D^*\Delta\delta)^2 + (D'^*\Delta\delta)^2} \qquad (32)$$

or when $D'^* = 0,\ \Delta\delta \ll 1$:

$$\varepsilon \approx \varepsilon_0 + \frac{2D^* x_\beta^* N\Delta\delta}{\beta^*}, \qquad (33)$$

where D^* and D'^* are the linear and angular dispersions at the stripper, $\delta = \dfrac{\Delta p}{p} = (1/\beta^2)\dfrac{\Delta E}{E}$ is the relative momentum spread and $x_\beta^* = \sqrt{\beta^*\varepsilon_0}$.

The transverse beam emittance growth is of big importance for the realization of the charge exchange injection in synchrotrons.

3. DYNAMIC VACUUM PROBLEMS

The intensity related vacuum instability was first observed in ISR by O. Gröbner and R. Calder [37]. The initial vacuum pressure in the proton–proton collider was 10^{-10} Torr. It was noticed that when the beam current had increased 4 A, the vacuum pressure started to rise reaching 10^{-7}–10^{-6} Torr level and the beam was destroyed (Fig. 21).

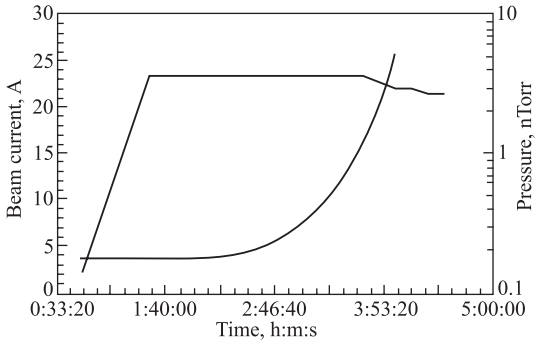

Fig. 21. Pressure instability during beam accumulation in the ISR [37]

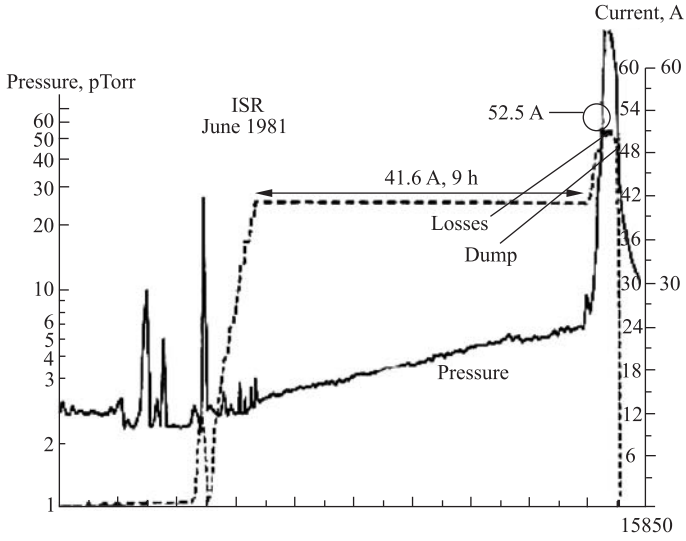

Fig. 22. ISR runaway-type pressure rise

Another case of runaway-type pressure rise in ISR is shown in Fig. 22.

The mechanism of this kind of pressure instability is believed to be the following [38, 39]. Accelerated proton beam ionizes the molecules of the residual

gas. A large number of electrons and positive ions are created. The ionization cross section $\sigma_{\rm ion}$ in m^2 for particles with charge $eZ_{\rm pr}$, moving with velocity $\beta = vc$ and hitting a residual gas molecules could be estimated by the formula:

$$\sigma_{\rm ion} = 1.874 \cdot 10^{-24} \, \frac{Z_{\rm pr}^2}{\beta^2} \, (Ax + B), \tag{34}$$

where A, B are coefficients, specific for the hit molecule and $x = 2 \ln (\beta\gamma) - \beta^2$.

The positive ions are repelled by the positive space charge of the beam towards the vacuum chamber walls. For protons, a typical beam potential is 100 V per 1 A. Hence, for high current machines the energy of the bombarding ions can reach several hundred eVs. This causes desorption of tightly bound surface gas. The outgassing increases the pressure in the vacuum chamber of the accelerator, which in turn leads to more intensive ionization. A positive feedback could be created. The phenomenon is schematically depicted in Fig. 23.

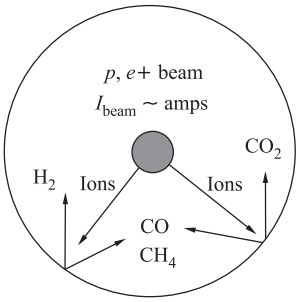

Fig. 23. Principle of ion induced pressure instability [39]

The ion induced pressure instability was one of the major factors limiting the stored proton beam intensity.

For room temperature vacuum systems, CO is the most dangerous component of the residual gas due to its large ionization cross section and to its high ion induced desorpion yield.

Let us look at the ion induced pressure instability in a more quantitative way. The outgasing flux Q in Torr $\cdot$ m$^3 \cdot$ s^{-1} for a slice dx of the vacuum chamber is:

$$Q = \eta \, \sigma \, \frac{I}{e} \, P \, dx + q_0 \, dx, \tag{35}$$

where η is the molecular desorption coefficient, i.e., the number of molecules released for an ion hitting the walls; σ is the residual gas ionization cross section; I — the total beam current; e — proton charge; P — vacuum pressure; q_0 — the specific thermal outgassing rate from the walls in Torr $\cdot$ m$^2 \cdot$ s^{-1}.

For the simplest linear vacuum system which consists of vacuum pumps with pumping speed S in m$^3 \cdot$ s^{-1} and which are spread through a distance L the critical beam current at which a pressure runaway starts is [39]:

$$(\eta \, I)_{\rm crit} = \frac{\pi^2 e c_0}{\sigma L^2}, \tag{36}$$

where c_0 is the specific conductance of the vacuum chamber in m$^4 \cdot$ s^{-1}.

Formula (36) is valid for conductance limited vacuum system, i.e., when the pumping speed S is large and the conductance c_0 is small.

The ion induced desorption yield η is $\eta = 1-8$ for nonbakable stainless steel vacuum system and strongly depends on the ion energy. For bakable vacuum system $\eta = 0.1-1.2$ (Fig. 24).

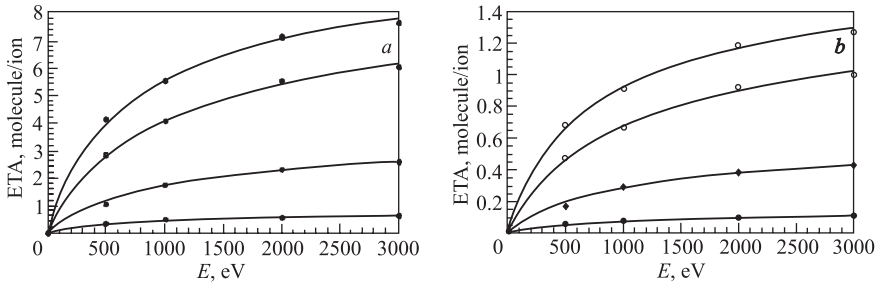

Fig. 24. Desorption yield for unbaked (a) and baked (b) stainless steel vacuum chamber [45]

The case of heavy-ion machines is quite different. In proton storage rings like ISR, the stored current is very high and the beam potential can reach up to 2 kV. On the contrary, in heavy-ion accelerators the beam potential is rather low. In LEIR it is about 10 V. In SIS-18 the space charge potential for U^{28+} at injection energy is about 50 eV. In such a weak electric field the residual gas ions are not accelerated enough to produce high desorption rate.

In spite of this pressure, bumps up to 10^{-9} Torr have been observed in LEAR during continuous injection of 10^8 ions/s (the initial static pressure in the machine was $5 \cdot 10^{-12}$ Torr) [40]. It was found that the outgassing of the vacuum equipment is due to the impact of lost Pb^{54+} ions — the so-called beam loss induced pressure rise.

Vacuum pressure instabilities were also observed in AGS Booster [41] and in SIS-18 [42].

In the ion collider RHIC during 2001 high-intensity Au run, when the intensity was raised beyond $8 \cdot 10^8$ ions/bunch, pressure rises of several decades were measured [43, 44]. The rapid pressure rises sometimes exceeded the control electronics threshold and the beam was aborted (Fig. 25). The pressure rise was especially prominent during 110-bunch gold injection. The pressure instability was recorded in the warm sections of the ion collider. The designed vacuum in these room temperature regions with overall length 1.4 km is less than $5 \cdot 10^{-10}$ Torr. Even 5% beam loss per 10 m gives rise to serious experimental background problems in the interaction regions.

There are several potential mechanisms that could cause the pressure instability in ion accelerators.

• Ion induced desorption caused by the primary beam loss. In synchrotrons the largest beam loss occurs during injection and RF-capture. The lost primary

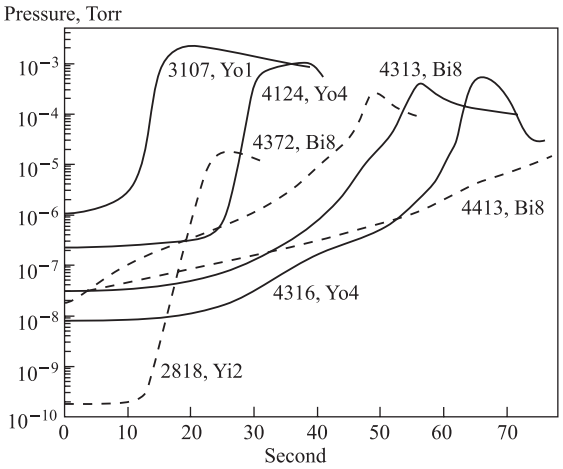

Fig. 25. RHIC pressure bumps during run 2003 and run 2004. All cases are for gold beams and unbaked vacuum chamber [45]

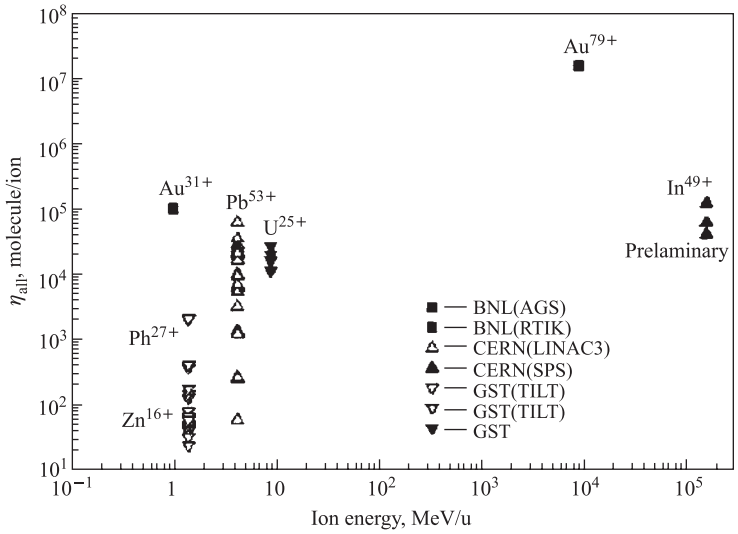

Fig. 26. Overview of ion induced desorption data obtained at BNL, CERN, and GSI

ions hit the vacuum chamber walls at grazing angles of mrad or less. In such hits more than 10^5 molecules can be released per lost ion. Indeed measurements at AGS Booster, LEAR, SIS-18 and RHIC show desorption rates as large as 10^5 and even 10^7 (Fig. 26).

• The charge exchange of beam ions with residual gas atoms and molecules is another potential source of large amount of lost ions. The beam ions that had lost or captured electrons leave the beam and hit the walls of the vacuum chamber at grazing angles. Such grazing-angle ion hits can desorb large amount of gas molecules and cause direct beam loss induced pressure instability.

• The pressure rise could be caused also by an electron cloud. The electrons in a cloud bombard the walls and could desorb gas molecules. The phenomenon is known as electron multipacting. This kind of pressure instability is sensitive to bunch intensity and to bunch spacing.

In the cryogenic vacuum systems, molecules are cryopumped with high efficiency directly on the cold walls.

The estimations made for LHC [46] pointed out that the critical beam current is:

$$(\eta I)_{\mathrm{crit}} = \frac{\pi}{2}\,\bar{v} s r_p \frac{e}{\sigma}, \tag{37}$$

where $\bar{v}$ is the mean molecular velocity; s is the sticking probability of molecules on the walls; σ — the ionization cross section; r_p — radius of the cold beam pipe.

For $s = 1$, the critical current becomes very large, in the order of kA. However, this optimistic value can be reduced to a great extent by condensed gas, especially H_2, accumulated on the cold bore, which can produce molecular desorption yield up to 10^4 molecules per ion.

The following measures could help to cope with vacuum pressure instability:

— very strict choice of materials and vacuum pumps; use of distributed pumping; negligible amount of leaks in the vacuum chamber;

— surface cleaning of the vacuum chamber walls by means of argon glow discharge;

— provision for bakeout in place up to 200 °C for 24 h;

— beam scrubbing;

— use at strategic locations of low outgassing materials as noble metal coatings or thin evaporated films of titanium;

— distributed pumping by ribbons of Non-Evaporable Getters (NEG) for increasing the local pumping speed;

— cooling of vacuum chamber walls.

4. INTRABEAM SCATTERING

The intrabeam scattering (IBS) phenomenon consists in multiple small-angle Coulomb scattering of particles within relativistic beams. The collisions between the particles in the beam couple the beam emittances in all three dimensions. This causes the beam size to grow.

The emittance growth due to the multiple Coulomb scattering in electron beams was first considered by H. Bruck and J. Le Duff [47].

For proton beams IBS was first analyzed by A. Piwinski in a more general treatment [48].

In early theoretical works averaged lattice functions have been used for simplicity. In a smooth lattice approximation the Hamiltonian in a frame, moving along with the synchronous particle (the so-called particle frame, PF), is independent of time, i.e., the dynamical system is conservative. The total beam temperature in PF is conserved.

Below the transition energy, $\gamma < \gamma_t$, when the beam is in the positive mass regime, the behavior of the beam particles is similar to that of a gas. Each degree of freedom exchanges energy with the others according to their relative temperatures. Because at the beginning of accelerator cycle the transverse temperature is higher than the longitudinal, a cooling in transverse planes takes place. Below the transition energy the beam can reach equilibrium between the transverse and longitudinal temperatures.

Such a behavior has not yet been observed in high energy rings.

The transverse temperature is:

$$kT_\perp = m_i c^2 \beta^2 \gamma^2 Q \frac{\varepsilon_\perp}{R}, \tag{38}$$

where m_i is the ion mass; Q — the betatron tune; $\varepsilon_\perp$ — transverse emittance; R — mean radius; β, γ — the relativistic factors. The transverse beam temperature is proportional to the transverse emittance.

The longitudinal temperature is determined by

$$k\,T_\parallel = m_i \beta^2 c^2 \Big(\frac{dp}{p}\Big)^2, \tag{39}$$

i.e., is proportional to the square of relative momentum spread.

Above the transition energy, $\gamma > \gamma_t$, due to the fact that the beam is in negative mass regime, interparticle collisions cause an exchange of energy from the directed motion of the relativistic beam into energy in all three directions. The beam grows in all three dimensions and no equilibrium exists. This can happen even in the case of uniform machine lattice.

It is the coupling between the longitudinal and the transverse motions via the dispersion in what a beam of particles in a circular accelerator differs from a gas of molecules. The border line between the regions where the coupling in the horizontal plane or the effect of longitudinally collapsed velocity distribution dominate is represented in [49]. It is determined by the condition that the contribution to the beam width due to betatron oscillations equals the contribution which is due to the coupling via dispersion, $(\varepsilon_x \beta_x)^{1/2} = D(\Delta p/p)$. To the right of this line the coupling may be neglected and IBS can in good approximation

be described by the gas-relaxation formulae. In particular this is true for high energies (above the transition). On the other hand, the coupling between the horizontal and the vertical motions (if exists) averages the growth rates in the transverse directions. The smooth lattice approximation is rough and has been later abandoned in favour of more realistic models that take into account the variation of the lattice functions around the ring [50, 51].

In real AG synchrotrons, the Hamiltonian is time-dependent and the total energy of the beam is not a constant of motion. Heat will be transferred between the beam and the structure. The AG lattice can emit phonons into the beam and heat it up [52].

In a strong focusing lattice, the sum of the emittances always arises. Although the emittance in a particular direction may, in principle, be reduced, this has not been observed in accelerator practice.

In Martini's paper, an improved Piwinski's model has been introduced. The paper of Bjorken and Mtingwa uses the S-matrix approach. This latter formalism is included in the MAD code.

Both Bjorken and Mtingwa's and Martini's models are in good agreement with one another. It is also commonly accepted that for high energies, i.e., above transition, Martini's and Bjorken and Mtingwa's models are able to describe IBS effect with accuracy better than 50%.

The price you must pay is that the calculations are computationally intensive.

Accurate computation of IBS effects can be performed only with computer simulations. Two widespread computer codes that could simulate IBS effects are: BETACOOL developed by I. Meshkov and co-workers [53] and SIMCOOL developed by V. Parkhomchuk and I. Ben-Zvi [54].

BETACOOL code calculates IBS taking into account the real lattice of the accelerator. It incorporates the Martini's model. SIMCOOL code is based on a treatment of the IBS based on the plasma approach.

Several approximate approaches that simplify the calculation of IBS effects have been devised. Very promising is the approach of J. Wei, who has succeeded in improving the accuracy and the speed of calculations [55].

For the case of nearly constant ratio $D/\sqrt{\beta_x}$, where D is the dispersion and β_x is the Twiss amplitude function, as is in a FODO lattice, J. Wei has simplified the formula for emittance growth rates to:

$$\begin{bmatrix} \frac{1}{\sigma_p}\frac{d\sigma_p}{dt} \\ \frac{1}{\sigma_x}\frac{d\sigma_x}{dt} \\ \frac{1}{\sigma_y}\frac{d\sigma_y}{dt} \end{bmatrix} = \frac{Z^4 N}{A^2}\frac{r_0^2 L_c c}{8\pi\gamma\varepsilon_x^*\varepsilon_y^*\varepsilon_l^*}F(\chi)\begin{bmatrix} n_b(1-d^2) \\ -\frac{a^2}{2}+d^2 \\ -\frac{b^2}{2} \end{bmatrix}, \tag{40}$$

where σ_x is the horizontal rms betatron amplitude; σ_y — the vertical rms betatron amplitude; σ_p — the fractional momentum deviation; Z — the ion charge state; A — the ion mass number; N for bunched beams is equal to the number of particles per bunch while for unbunched beams it is equal to the total number of particles; r_0 is the classical proton radius; L_c is the Coulomb logarithm, $L_c = \ln(b_{\max}/b_{\min}) = \ln(2/\theta_{\min})$, $b_{\min}$ and $b_{\max}$ being the minimum and maximum impact parameters, $\theta_{\min}$ being the minimum scattering angle, approximately $L_c \approx 20$. In (40) ε_x^*, ε_y^* are the normalized transverse rms emittances, and ε_l^* is the normalized longitudinal rms emittance.

$$\varepsilon_{x,y}^* = \beta\gamma\frac{\sigma_{x,y}^2}{\beta_{x,y}}, \tag{41}$$

$$\varepsilon_l^* = \beta\gamma\sigma_p\sigma_s, \tag{42}$$

where σ_s for bunched beams is equal to the bunch rms length, while for unbunched beams it equals $\sqrt{\pi}R$;

$$n_b = \begin{cases} 1 \text{ for bunched beam,} \\ 0 \text{ otherwise,} \end{cases} \tag{43}$$

$$d = \frac{D\sigma_p}{\sqrt{\sigma_x^2 + D^2\,\sigma_p^2}} < 1, \tag{44}$$

$$a = \frac{\beta_x d}{D\gamma}, \tag{45}$$

$$b = \frac{\beta_y\sigma_x}{\beta_x\sigma_y}\,a. \tag{46}$$

In (40), $F(\chi)$ is defined analytic function. $F(\chi)$ is a smooth function of χ, it is positive when $\chi < 1$, zero when $\chi = 1$, and negative when $\chi > 1$ (Fig. 27)

$$\chi = \frac{a^2 + b^2}{2}. \tag{47}$$

The emittance growth rates are proportional to the particle density in the 6D phase space $N_b/(\varepsilon_x^*\,\varepsilon_y^*\,\varepsilon_l^*)$ and are inversely proportional to the particle energy. For heavy ions the factor Z^4/A^2 is of big importance.

The J. Wei simplified description has been tested with Au ions at RHIC [56]. At store energy, i.e., above transition, the measurements and the calculations agree rather well both for the bunch length and for the transverse emittances growth rates. At injection energy, i.e., below transition, the agreement between the theory and the experiment is a bit worse for the bunch lengh growth rate. But whereas the theory gives a slight decrease of the transverse emittances, the

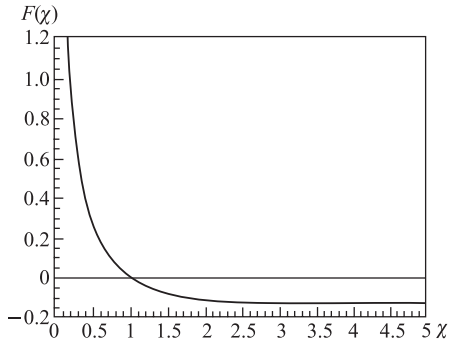

Fig. 27. Function $F(\chi)$

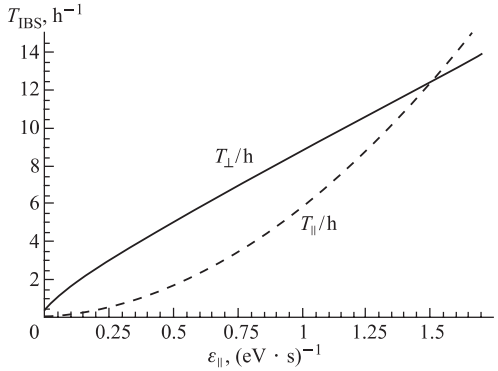

Fig. 28. Emittance growth times due to IBS as a function of the longitudinal emittance; $_{208}Pb^{82+}$ ions at injection from the SPS. The solid line represents the growth time for the horizontal emittance; while the dashed line, for the longitudinal emittance [58]

measurements have always shown a growth. This growth has been linear in time. For that reason, the authors have considered that a diffusion process due to strong noise source has been observed.

It is the IBS that is the most severe drawback which restricts the average luminosity in RHIC [56]. This is due to the high charge state of the gold ions. At injection into RHIC, the IBS growth time for the momentum spread is about 3 min. Emittances in both the longitudinal and the transverse dimensions grow up. IBS limits beam and luminosity lifetimes and leads to particle loss out of the RF buckets.

Beam cooling must be applied to cope with luminosity reduction. At RHIC R&D works are under way for bunched beam electron cooling at collision energy [57]. The electron cooling system is based on an energy recovering linac. The electron beam will be with the energy of 54 MeV and current 100–200 mA.

Ten times increase of the average luminosity is anticipated.

The calculated IBS growth times for LHC lead ion beams of nominal intensity at injection from the SPS are shown in Fig. 28.

5. PROCESSES IN NUCLEAR INTERACTIONS OF ULTRA-RELATIVISTIC HEAVY IONS

The Large Hadron Collider (LHC) at CERN, which is going to start accelerating and colliding proton beams at maximum energy of 2×7 TeV in mid 2008, will also run as ion collider. In the so-called lead programme, LHC will collide $_{208}\mathrm{Pb}^{82+}$ beams at a maximum energy of 2.75 TeV/u with peak luminosity $L = 10^{27}\ \mathrm{cm}^{-2} \cdot \mathrm{s}^{-1}$.

During the design works on LHC as a led ion collider it was realized that the collisions of high-energy ions are source of secondary beams of ions with charge states and mass numbers that differ from reference values [58]. These secondary ion beams are originated in the interaction points and further they are bent by the magnetic structure in a wrong way and finally hit one of the downstream superconducting magnets (Fig. 29). This concentrated source of hit may lead to a quench.

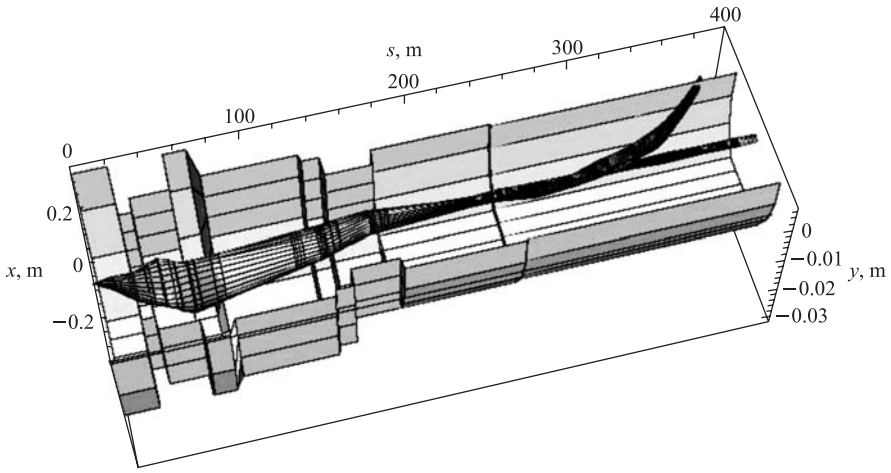

Fig. 29. Main beam of $_{208}\mathrm{Pb}^{82+}$ ions and the secondary beam of $_{208}\mathrm{Pb}^{81+}$ ions emerging from IP2 of the LHC as a lead ion collider [58]

The strong chromatic effect caused by the low-β quadrupoles makes the secondary beam dynamics complicated. Detailed tracking calculations with 3D codes are necessary [59].

For heavy ions with $Z_{\rm pr} \geqslant 30$ two electromagnetic interactions are considered as very dangerous because they change the charge state or mass of the colliding ions.

5.1. Electron Capture from Pair Production (ECPP). This process consists in production of e^+e^- pair and a subsequent capture of the electron by one of the colliding nuclei:

$$_{208}\mathrm{Pb}^{82+} + {}_{208}\mathrm{Pb}^{82+} \xrightarrow{\gamma} {}_{208}\mathrm{Pb}^{82+} + {}_{208}\mathrm{Pb}^{81+} + e^+. \tag{48}$$

The detailed theoretical estimations give for the cross section the value: $\sigma_{\rm ECPP} \approx 281$ b [60].

The quench limit for heavy ions with energy per nucleon T_n is equal to that for protons with kinetic energy $T = T_n$ divided by the mass number A. In LHC this quench limit for Pb ions is $8 \cdot 10^4$ m/s. On the other hand, the flux of secondary $_{208}\mathrm{Pb}^{81+}$ ions can be derived from the collider luminosity. For $L = 10^{27}$ cm$^{-2}\cdot$ s^{-1} the flux of $_{208}\mathrm{Pb}^{81+}$ ions is $2\cdot 10^5$ m/s, i.e., twice the quench limit — the ECPP effect could be very dangerous. It is considered as one of the main luminosity limiting factors in LHC lead ion collider.

The heavy-ion collider RHIC at BNL seems luckier. RHIC collides fully stripped gold nuclei at 100 GeV/u energy. When the main beam consists of $_{179}\mathrm{Au}^{79+}$ ions the secondary beam created in ECPP effect will consists of $_{179}\mathrm{Au}^{78+}$ ions. Fortunately, $_{179}\mathrm{Au}^{78+}$ ions still lie within the RHIC momentum aperture. Therefore, $_{179}\mathrm{Au}^{78+}$ ions are lost gradually and don't hit the accelerator at a localized spot. For that reason, in RHIC the deposited by the secondary beam energy doesn't cause any problems.

5.2. Electromagnetic Dissociation (EMD). This is a two stages process. In the first stage the lead nucleus is excited. In the second stage it decays via neutron emission:

$$_{208}\mathrm{Pb}^{82+} + {}_{208}\mathrm{Pb}^{82+} \xrightarrow{\gamma} {}_{208}\mathrm{Pb}^{82+} + {}_{208}\mathrm{Pb}^{82+*} \to {}_{208}\mathrm{Pb}^{82+} + {}_{207}\mathrm{Pb}^{82+} + n. \tag{49}$$

Computer simulations estimate the EMD cross section at LHC lead beam energy as $\sigma_{\rm EMD} \approx 104$ b [61].

To cope with these adverse effects special collimators must be placed in points where the main and the secondary beams are well separated.

REFERENCES

1. *Keller R.* // GSI Ann. Rep. 1987. P. 360.
2. *Reich H., Oks E. M., Spädtke P.* // Rev. Sci. Instr. 2000. V. 71. P. 707.
3. *Leitner D., Lyneis C. M.* // Proc. of 2005 Part. Accel. Conf., Knoxville, Tennessee, 2005. P. 179.

4. *Beebe E. et al.* // Proc. of Eur. Part. Accel. Conf. «EPAC'02», Paris, 2002. P. 281.
5. *Donets E. D.* // Rev. Sci. Instr. 2000. V. 71. P. 810.
6. *Hedblom K. et al.* // 3rd Eur. Part. Accel. Conf. «EPAC'92», Berlin, 1992. P. 462.
7. *Blasche K., Franzke B.* // Proc. of Eur. Part. Accel. Conf. «EPAC'94», London, 1994. P. 133.
8. *Bär R. et al.* // Proc. of Eur. Part. Accel. Conf. «EPAC'98», Stockholm, 1998. P. 499.
9. *Ratzinger U.* // Proc. of Eur. Part. Accel. Conf. «EPAC'00», Vienna, 2000. P. 98.
10. *Chanel M.* // Proc. of Eur. Part. Accel. Conf. «EPAC'02», Paris, 2002.
11. *Beuret A. et al.* // Proc. of Eur. Part. Accel. Conf. «EPAC'04», Lucerne, 2004. P. 1153.
12. *Kovalenko A. D.* // Proc. of Eur. Part. Accel. Conf. «EPAC'00», Vienna, 2000. P. 554.
13. *Fischer W.* // Proc. of Eur. Part. Accel Conf. «EPAC'06», Edinburgh, 2006.
14. *Donets E. E., Donets E. D., Syresin E. M.* // Proc. of Rus. Part. Accel. Conf. «RuPAC-XIX», Dubna, 2004. P. 453.
15. *Bohr N.* // Kgl. Danske Videnskab. Mat., Fys., Medd. 1948. V. 18, No. 8.
16. *Nikolaev V. S. et al.* // Zh. Techn. Fiz. 1978. V. 48. P. 1399.
17. *Franzke B.* // IEEE Trans. Nucl. Sci. 1981. V. NS-28. P. 2116.
18. *Madsen N.* Preprint CERN, PS/DI Note 99-21. 1999.
19. *Smolyakov A., Spiller P.* Preprint GSI 51-1. Darnstadt, 2006.
20. *Bransden B. H.* Atomic Collision Theory. 2nd Ed. Benjamin Press, 1983.
21. *Oppenheimer J. R.* // Phys. Rev. 1928. V. 31. P. 349.
22. *Schlachter A. S. et al.* // Phys. Rev. A. 1983. V. 27. P. 3372.
23. CERN Heavy-Ion Facility Design Report / Ed. Warner D. CERN-93-01. Geneva, 1993.
24. *Roser T., Ahrens L. A., Hseuh H. C.* // 4th Eur. Part. Accel. Conf. «EPAC'94», London, 1994. P. 2441.
25. *Teplova Ya. A., Dmitriev I. S., Belkova Yu. A.* // Nucl. Instr. Meth. B. 2000. V. 291. P. 164–165.
26. *Nikolaev V. S.* // Usp. Fiz. Nauk. 1965. V. 85. P. 679.
27. *Betz H. D.* // Rev. Mod. Phys. 1972. V. 44. P. 465.
28. *Fettouhi A.* PhD Thesis. Giesen, 2006.
29. *Toleberger P. et al.* // IEEE Trans. Nucl. Sci. 1985. V. NS-32. P. 1767.
30. *Nikolaev V. S., Dmitriev I. S.* // Phys. Lett. A. 1968. V. 28. P. 277.
31. *Roser T.* // 4th Eur. Part. Accel. Conf. «EPAC'94», London, 1994. P. 151.
32. *Bethe H. A., Ashkin J.* Experimental Nuclear Physics / Ed. E. Segre. V. 1. N. Y.: John Wiley, 1959.
33. *Rozet J. P., Stephan C., Vernhet D.* // Nucl. Instr. Meth. B. 1996. V. 107. P. 67.

34. *Joy J.* // Nucl. Instr. Meth. 1973. V. 106. P. 237.

35. *Franzke B.* // CAS – Fourth Adv. Accel. Phys. Course (CERN 92-01). Noordwijkerhout, Netherlands, 1991. P. 100.

36. *Hedblom K., Frissel D. L.* // Sixteenth Part. Accel. Conf., Dallas, 1995. P. 1861.

37. *Gröbner O., Calder R.* // Part. Accel. Conf., San Francisco, 1973. P. 760.

38. *Fischer E.* // IEEE Trans. Nucl. Sci. 1977. V. NS-24, No. 3. P. 1227.

39. *Gröbner O.* Dynamic Outgassing // CAS Vacuum Technology. CERN 99-05. Snersten, Denmark, 1999.

40. *Mahner E. et al.* // Phys. Rev. ST-AB. 2003. V. 6. P. 013201.

41. *Zhang S. Y., Ahrens L. A.* // Part. Accel. Conf., New York, 1999. P. 3294.

42. *Kramer A. et al.* // Proc. of Eur. Part. Accel. Conf. «EPAC'02», Paris, 2002. P. 2547.

43. *Fisher W. et al.* // Ibid. P. 1485.

44. *Hseuh H. C., Smart L. A., Zhang S. Y.* // Ibid. P. 2559.

45. *Zhang S. Y.* BNL Preprint C-A/AP/190. 2005.

46. *Collins I. R. et al.* // Intern. Workshop on Performance Improvements of e^+e^- Factories, KEK, Japan, 1999.

47. *Bruck H., Le Duff J.* // Intern. Conf. on High Energy Accelerators. Frascati, 1965.

48. *Piwinsky A.* // Proc. of CERN Accel. School, Gif-sur-Yvette, Paris, 1984. CERN 92-01. P. 405.

49. *Sorensen A.* // CAS, Second General Accel. Phys. Course, Aarhus, 1986. P. 135.

50. *Martini M.* CERN Preprint No. PS/84-9. Geneva, 1984.

51. *Bjorken J., Mtingwa S.* // Part. Accel. 1983. V. 13. P. 115.

52. *Li X.-P., Sessler A. M., Wei J.* // Proc. of Eur. Part. Accel. Conf. «EPAC'94», London, 1994. P. 1379.

53. *Meshkov I. et al.* Physics Guide of BETACOOL Code. Version 1.1. BNL Report C-A/AP/262. 2006.

54. *Parkhomchuk V., Ben-Zvi I.* BNL C-A/AP/47. 2001.

55. *Wei J.* // Proc. of 1993 Part. Accel. Conf., Washington, 1993. P. 3651.

56. *Fischer W. et al.* // Proc. of Eur. Part. Accel. Conf. «EPAC'02», Paris, 2002. P. 236.

57. *Fischer W.* // 2005 Part. Accel. Conf., Knoxville, Tennessee, 2005. P. 122.

58. The LHC Design Report (Chapter 21). CERN-2004-003. Geneva, 2004.

59. *Jowett J. M. et al.* // Proc. of Eur. Part. Accel. Conf. «EPAC'04», Lucerne, 2004. P. 578.

60. *Meier H. et al.* // Phys. Rev. A. 2001. V. 63. P. 032713.

61. *Pshenichnov I. A. et al.* // Phys. Rev. C. 2001. V. 64. P. 024903.